Eur. Phys. J. C (2024) 84:981
https://doi.org/10.1140/epjc/s10052-024-13325-0

THE EUROPEAN PHYSICAL JOURNAL C

Regular Article - Experimental Physics

Detection response of the active components of the SciBar Cosmic Ray Telescope at Sierra Negra

F. Monterde-Andrade[1], L. X. González[1,2,a], J. F. Valdés-Galicia[1], O. G. Morales-Olivares[3,13], M. A. Sergeeva[2], J. Newton-Bosch[1], E. Ortiz[3], A. Hurtado[1], R. Taylor[1], Y. Matsubara[4], T. Sako[5], Y. Itow[6], T. Kawabata[6], K. Munakata[7], C. Kato[7], Y. Hayashi[7], Y. Masuda[7], M. Matsumoto[7], H. Takamaru[8], S. Shibata[4], A. Oshima[4], T. Koi[4], H. Kojima[4], H. Tsuchiya[9], K. Watanabe[10], M. Kozai[11], Y. Nakamura[12]

[1] Instituto de Geofísica, Universidad Nacional Autónoma de México, 04510 Ciudad de México, Mexico
[2] LANCE/SCiESMEX. Instituto de Geofísica, Unidad Michoacán, Universidad Nacional Autónoma de México, 58190 Morelia, Michoacán, Mexico
[3] Escuela Nacional de Ciencias de la Tierra, Universidad Nacional Autónoma de México, 04510 Ciudad de México, Mexico
[4] Center for Muon Science and Technology, Chubu University, Matsumoto, Kasugai, Aichi 487-8501, Japan
[5] Institute for Cosmic Ray Research, University of Tokyo, Kashiwanoha, Kashiwa, Chiba 277-8582, Japan
[6] Institute for Space-Earth Environmental Research, Nagoya University, Chikusa, Nagoya, Aichi 464-8601, Japan
[7] Faculty of Science, Shinshu University, Asahi, Matsumoto, Nagano 390-8621, Japan
[8] College of Engineering, Chubu University, Matsumoto, Kasugai, Aichi 487-8501, Japan
[9] Japan Atomic Energy Agency, Tokai, Naka-gun, Ibaraki 319-1184, Japan
[10] National Defense Academy of Japan, Hashirimizu, Yokosuka, Kanagawa 239-8686, Japan
[11] Joint Support-Center for Data Science Research, Research Organization of Information and Systems, Midori-cho, Tachikawa, Tokyo 190-0014, Japan
[12] Institute of High Energy Physics, Chinese Academy of Sciences, Yuquan Road, Shijingshan District, Beijing 100049, China
[13] Facultad de Ciencias en Física y Matemáticas, Universidad Autónoma de Chiapas, Boulevard Belisario Domínguez, 29050 Tuxtla Gutiérrez, Chiapas, México

Received: 20 June 2024 / Accepted: 4 September 2024
© The Author(s) 2024

Abstract The Scibar Cosmic-Ray Telescope (SciCRT) is the most promising detector of the Sierra Negra Cosmic Rays Observatory (SN-CRO). At this location, being a target and a tracker of secondary cosmic rays, the SciCRT offers a high probability of observing solar energetic particles and lower energy galactic cosmic rays (LEGCR); also, it allows the identification of incoming particles by measuring their energy deposition. In this work we present a Geant4-based simulation of the energy deposited by neutrons, γ-rays, protons, electrons and muons in the optimally running SciCRT components. We also calculated the detection efficiency of the SciCRT at its current state. Our simulation results provide new information about the SciCRT detection response that may be used as a basis to estimate and analyze the energy spectra of primary particles.

1 Introduction

Observation of the particles accelerated during a solar flare has motivated the development and design of new detectors. Specifically, there is special interest in detecting the solar neutrons (n_s) released as a product of a flare due to their ability to travel towards the Earth at relativistic velocities unmodulated by the coronal, interplanetary and terrestrial magnetic fields, [1]. Neutrons undergo β-decay after about 14.6 min [2]; however, if simultaneous n_s and γ-ray emission is assumed for a flare, n_s with kinetic energy E = 1 GeV would reach 1 AU just 1 min after γ-rays and would be delayed 11 min with E = 100 MeV. Such properties makes them an ideal candidate for the study of charged particle dynamics at the flare locality because they carry unaltered information regarding the particle source region, [3]. If these high energy n_s reach the Earth's atmosphere, they act as a primary cosmic ray (CR) and produce an extensive air shower (EAS) of secondary particles comprising electromagnetic, muonic and hadronic components, [4]. On that basis, in order to detect the hadronic component of the EAS associated with an Earth-

[a] e-mail: xavier@igeofisica.unam.mx (corresponding author)

Published online: 27 September 2024

directed emission of n_s at ground level, there are two major network of detectors; these correspond to the global networks of Neutron Monitors (NM) and Solar Neutron Telescopes (SNT). Historically, both the NM's and SNT's have successfully detected 12 n_s events since the Solar Cycle (SC) 23, [5–7]; nevertheless, significant design improvements regarding determination of particle directionality and energy resolution are needed in order to better characterize the n_s energy spectra at the production region and hence the acceleration mechanism of charged particles. In addition, due to the geomagnetic field, high cut off rigiditiy regions in low latitudes are only reachable by particles with a given minimum energy; therefore, a near-equatorial observation site is desirable since it minimizes the noise from the background of low energy secondary CR and ensures that particles with a given minimum energy are being detected. High mountain locations are, moreover, required in order to minimize the absorption of particles in the atmosphere, thereby increasing the probability of detecting the hadronic component of EAS generated by n_s.

Located at the summit of Mt. Sierra Negra, in Puebla, Mexico (19.0 N, 97.3 W), the Sierra Negra Cosmic Rays Observatory (SN-CRO) is a unique site for the observation of galactic CR and solar energetic particles because of its altitude (4580 m a.s.l.) and high cut off rigidity (8.24 GV). At its current state, the SN-CRO comprises the Solar Neutron Telescope of Sierra Negra (SNT-SN) [8,9], a meteorological station intended to monitor atmospheric effects [10], and the Scibar Cosmic-Ray Telescope (SciCRT), [11].

The SciCRT project was proposed as a novel and more efficient detector intended to observe the secondary CR associated with the n_s emitted at the locality of a solar flare [12]. Such design would outdo the SNT-SN ability to estimate particles arrival direction and its energy discrimination channel system, [8]. Originally called Scibar (Scintillation Bars), the SciCRT was developed in 2003 for the KEK to Kamioka (K2K) neutrino oscillation experiment in Japan [13] and was later used in the SciBoone experiment at the Fermi National Accelerator Laboratory (FNAL), [14]. After completing its goal in the FNAL experiments, in April, 2013, the SciCRT was installed at the SN-CRO and started operating in September, 2014.

Given the SN-CRO location, a high flux of secondary CR constantly impinges on the SciCRT. This flux initially exceeded the readout capabilities of the SciCRT's original data acquisition system; hence, modifications for performance optimization have been applied since 2015, [15]. The changes include the installation of 9 additional Back End Boards (BEBs), allowing to increase the data transfer rate threshold, from 0.4 to 3.3 kHz; however, the modifications were not applied to all of the SciCRT components, [11]. The modified components are the main subject of our simulation; therefore, they should henceforth be understood as the active components of the SciCRT and correspond to the superblock 3 (SB3) and the muon layers (ML). This terminology and the SciCRT operating principles are explained in Sect. 2. We describe the set up of our simulation in Sect. 3 and discuss our results in Sect. 4. Finally, the concluding remarks of this work are summarized in Sect. 5.

2 The SciBar Cosmic Ray Telescope

The SciCRT is able to observe the lower energy galactic cosmic rays (LEGCR) background; however, its main goal is the detection of particles associated with solar flares. Due to its design, the SciCRT acts a a tracker and a target of secondary CR; thus, the path of an impinging particle can be tracked by measuring its energy deposition inside the detector volume. This enhances the capabilities for particle identification and rejection of background particles, [16]; in addition, when compared to the SNT-SN, the SciCRT has a larger effective area and a broader energy resolution, [11].

2.1 Detector design and operating principle

The SciCRT consists of an array of 14,848 scintillation bars (2.5 cm × 1.3 cm × 300 cm), composed of polystyrene doped with PPO (1%) and POPOP (0.03%), coated with a reflective layer of TiO_2 (0.25 mm thickness); together, these materials represent the plastic scintillator of which the bars are made up. All the bars are arranged in pairs of plates, stacked orthogonally, to represent the SciCRT coordinates. The plates representing the X coordinates (lower plates) and Y coordinates (upper plates) consist of 116 and 118 bars, respectively (Fig. 1a). The complete array is a stack of 128 plates divided into 8 substructures called superblocks (SB). Each of the 8 SBs are supported by steel frames (5 mm thickness) and a steel tube (3.8 mm thickness) to prevent the bottom bars from bending under the weight of the upper plates. There is a gap (82 mm) between the bottom surface of one SB and the top surface of the adjoining SB. Every scintillation bar has a hole (1.8 mm diameter) along its horizontal axis, inside of which a Wavelength Shift (WLS) fiber is inserted. These fibers are of the Y11(200)MS type (1.5 mm diameter), designed by Kuraray, and are connected to one of the 64 channels of the photocathode of a Multi-Anode Photomultiplier Tube (MAPMT), model H8804, developed by Hamamatsu Photonics (Fig. 1); thus, each SB is coupled to 29 MAPMT. The end of the WLS fibers connected to the bars is painted white to improve light collection efficiency, [11].

Upon reaching the detector, secondary particles interact with the atomic structure of the scintillation bars and transfer kinetic energy; as a result, an excited state is reached and photons are emitted afterwards. Such photons are emitted isotropically by fluorescence in the bars and may be

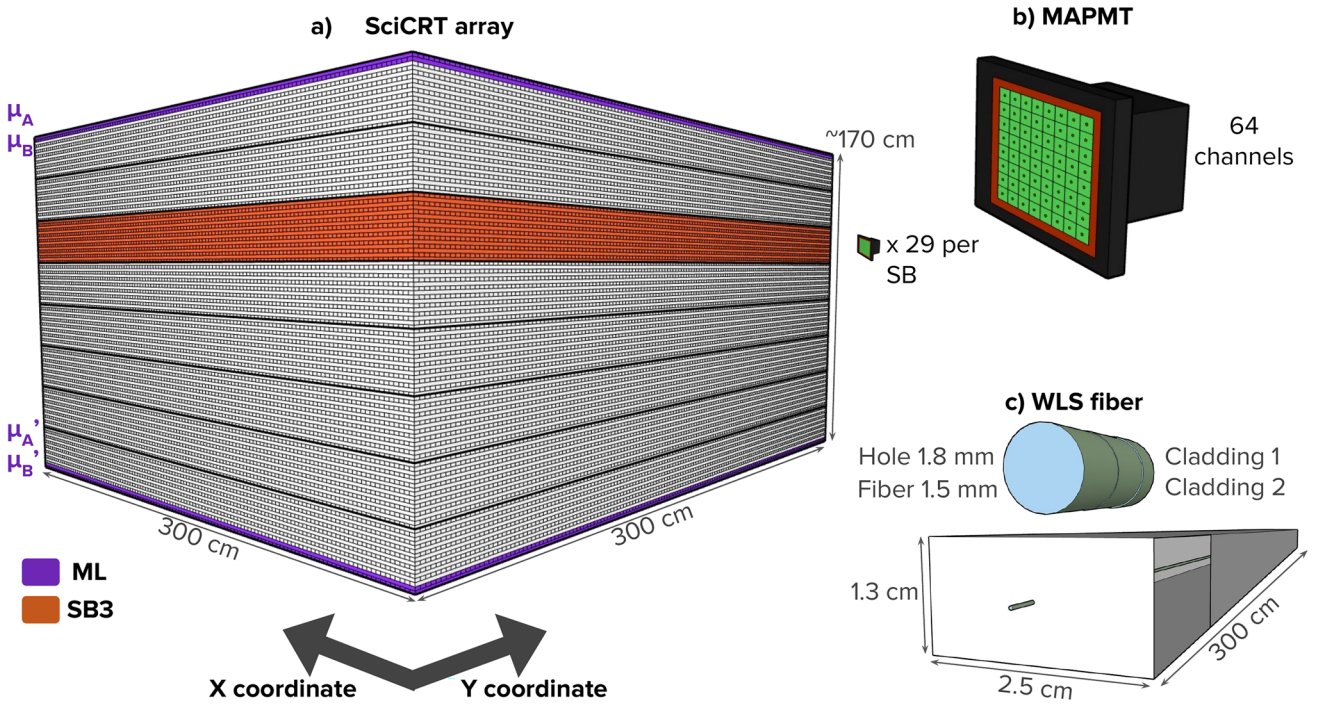

Fig. 1 Diagram of the SciCRT components. A total of 8 superblocks (SB), constitute the main volume of the SciCRT. The ML μ_A, μ_B, μ_A' and μ_B' correspond to the top plates of the SB1 and the bottom plates of the SB8, respectively. The orthogonal placement of the plates allows to define both X and Y coordinates. Being the SciCRT active components, these ML and the SB3 are shown highlighted in purple and orange, respectively (**a**). Each scintillation bar is connected to the photocatode of a MAPMT (**b**). A WLS fiber is embedded in a hole (1.8 mm diameter) along the horizontal axis of each bar, the fiber consists of a core with two claddings (**c**)

absorbed in the core of the WLS fibers, [17]. The core, made of polystyrene with a fraction of fluorine (200 ppm) and a refractive index of 1.59, is enveloped by an intermediate cladding of polymethylmethacrylate (PMMA) and an outer cladding of fluorinated PMMA with refractive indices of 1.49 and 1.42, respectively (Fig. 1c). On the basis of these properties, the fiber core is able to absorb (with absorption peak at 430 nm) the photons emitted by the bars and produce a wavelength shift. In this way, the WLS fibers collect, re-emit and drive the scintillation photons towards their end connected to the MAPMT, where the detection is finally achieved according to the quantum efficiency (QE). The maximum quantum efficiency of the MAPMT's is QE = 25%.

In order to detect muons, the ML are placed at the top of the superblock 1 (SB1) and the bottom of the superblock 8 (SB8) as a coincidence system; in this manner, the top ML are labeled as μ_A (upper plate) and μ_B (lower plate) and the bottom ML as μ_A' (upper plate) and μ_B' (lower plate), respectively (Fig. 1a). Muons can ionize the plastic of the scintillation bars, this interaction lead to the emission of scintillation photons that may hit the MAPMT's and produce a signal; however, since muons may traverse the whole detector without interacting, an event is recorded only if a trigger signal is received from all four ML.

Secondary neutral particles, like γ-rays and neutrons, do not ionize the plastic and hence do not generate scintillation light directly. Instead, secondary γ-rays require the production of electron-positron pairs. Pair production is a dominant process for γ-rays with energies E $\sim$ 100 MeV interacting with a nuclear electrostatic field, [18]. In this case, the nuclear electorstatic field is provided by the atoms in the organic molecules of the plastic; thus, impinging secondary γ-rays are able to produce pairs that will transfer energy to the electronic sturcture of the plastic. As a result, scintillation light will be emmited [17] and may be directed through the WLS fibers to the MAPMT's.

On the other hand, impinging secondary neutrons produce a recoil proton via a charge-exchange process (n, p) when they interact with the hydrogen nuclei in the organic molecules of the plastic. The resulting recoil proton will transfer energy through collisions and ionization, leading to excitation of the electronic structure of the bars. These electrons will emit scintillation light through fluorescence thereafter, [19,20]. As recoiled protons will be scattered with an angle Θ, the energy of the impinging neutron (E_n) is proportional to the energy deposited in the bars by the recoiled proton (E_p) according to, [21]:

$$E_p = E_n cos(\Theta). \quad (1)$$

Scattering between secondary neutrons and carbon nuclei (n, C) is also present within the plastic scintillator; however, the energies of the recoil carbon nuclei peak at $0.35E_n$. On the other hand, for the (n, p) process, the entire secondary neutron energy is transferred in a head-on collision ($E_p = E_n$), [19]; therefore, the secondary neutron detection is dominated by the recoil proton method. Furthermore, secondary neutrons transfer about 20–100% of their energy to the recoil protons when they impinge the SciCRT with energies between E_n = 100 MeV and E_n = 1000 MeV and up to about 15% for energies between E_n = 1000 MeV and E_n = 10000 MeV, [15].

In this way, through the mentioned mechanisms, an impinging particle may lead to scintillation emission in more than one bar; thus, the track of the particle inside the SciCRT can be reconstructed when such light, coming from different bars, is processed at the MAPMT. According to [11], hadronic tracks are similar in shape to particle showers and display a broader scattering. These are expected for the arrival of secondary neutrons and protons. On the other hand, electromagnetic tracks are narrow in shape and are expected for secondary γ-rays, electrons and muons. Due to such track reconstruction capability, an accurate analysis of particle directionality is possible; in addition, the intensity of the scintillation light recorded by the MAPMT is proportional to the energy deposited by an impinging particle in the SciCRT.

3 Simulation of the active components

3.1 Previous SciCRT simulations

The track analysis method for particle identification was developed on the basis of simulations of the Mini-SciCR, the SciCRT prototype, [17]. Once the SciCRT started operating, simulations of the particle tracks inside the SB's and its experimental validation were carried out; furthermore, calculations of the SciCRT effective area were performed for secondary neutrons, γ-rays and muons, [11]. This simulation considered 5/8 of the full SciCRT; however, it included the original electronics of the SciCRT and its limitations. A simulation of the scintillation light propagation in the WLS fibers and MAPMT was conducted, on the basis of the method developed in [22], as part of the design and implementation of the new fast read out system of the SB3 and ML, [23]. Nevertheless, this simulation focused on a single scintillation bar coupled to a WLS fiber and a MAPMT and this did not allowed to simulate the propagation of neutrons inside the SciCRT; moreover, the muon anticoincidence system was not included.

Even after all of this progress, there are other physical information that can be inferred from simulations of the detector. For instance, after a solar flare, having knowledge of the energy deposition of the associated particles impinging a detector and their energies over the Earth's atmosphere may allow to estimate the spectrum of charged particles at the solar atmosphere, [24,25]. Also, the detection efficiency for different particle species has not been calculated for the SciCRT. Thus, our work focuses in the simulation of the response of the active components of the SciCRT to the detection of secondary CR given an injection energy (E_{inj}). In the following section, we explain our methodology in further detail.

3.2 CORSIKA simulation

Neutrons, γ-rays, protons and electrons were selected as the input particles for our simulation of the SB3; likewise, we used muons for the simulation of the ML. We performed a CORSIKA simulation of the shower cascade, [26], in order to corroborate that there is a significant flux of these particles, at the SN-CRO altitude (h), that may be detected by the SciCRT. The set up of this simulation is analogous to the ones developed in [25,27]; there, further details regarding the CORSIKA operation can be found. Figure 2 displays the simulated fluxes of secondary photons, electrons, positrons, muons, protons and neutrons at Mt. Sierra Negra (SN) produced by primary CR protons, following a power law with spectral index j = - 2.7, with an energy range from 10 GeV to 10^6 GeV and an angular distribution from 0° to 60°. It is noteworthy that the resulting secondary CR are able to reach the atmospheric depth (X(h)) of the SN-CRO (X(h) = 575 g/cm^2, indicated with a vertical dashed line in Fig. 2) and penetrate deeper into the Earth's atmosphere. The peak of the muonic and electromagnetic components take place at h $\sim$ 15 km (approximately X(h) = 210 g cm^{-2}) and the vertical development of the shower is consistent with experimental data, [28].

3.3 Geant4 simulation

The response of a detector to its interaction with different particle species in different energy ranges may be studied by performing Monte Carlo simulations. This task can be accomplished with programming tools, such as Geometry and Tracking (Geant4) from CERN, [29]. For this work we used the Geant4 toolkit (version 11.2.1) in a multithread configuration. We simulated all the scintillation bars of the SciCRT in the Geant4 graphical user interface and arranged them according to Fig. 1a. As described in Sect. 2, each bar have a hole whereby a WLS fiber is embedded on one end and coupled to a MAPMT on the other. We specified the emission spectrum of the scintillation bars reported in [23,30] with peak emission at 420 nm and set their light yield as 8000 photons/MeV. Furthermore, we used a fast time constant of 3.6 ns and a bulk attenuation length equal to 250 cm.

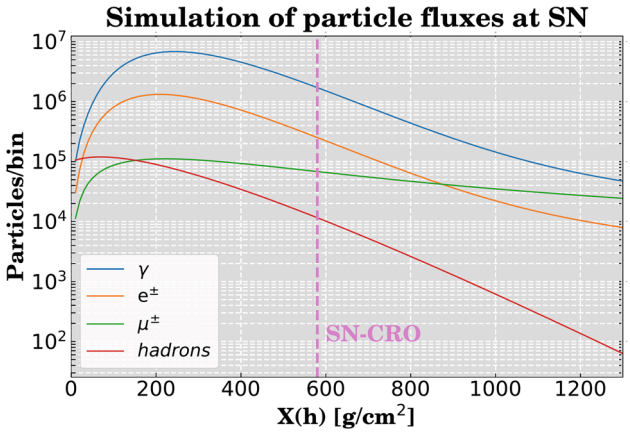

Fig. 2 CORSIKA simulation of the secondary CR flux through the Earth's atmosphere produced by primary CR protons, following a power law with spectral index j = -2.7, with an energy range from 10 to 10^6 GeV and an angular distribution from 0° to 60°. A significant flux is able to propagate to the SN-CRO location at X(h) = 575 g/cm^2 (vertical dashed line) and into deeper atmospheric depths (X(h))

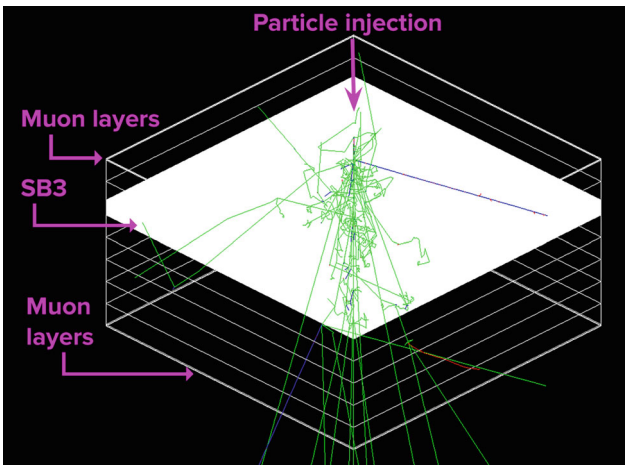

Fig. 3 Visualization of our SciCRT simulation in Geant4, the active components are highlighted. This figure shows the scintillation light emission (green lines) after the injection of 10 neutrons over the top of the detector. The blue and red lines correspond to positive charged and negative charged particles, respectively, produced inside the scintillation bars

Regarding the physical processes, we took into account classic electromagnetic processes: ionization, Bremsstrahlung, multiple scattering, pair production, Compton scattering and photoelectric effect. In order to account for particle interactions in the energy range E < 10^3 MeV, we included the QBBC model, [31], interactions above that value were handled under the FTFP_BERT model, [32]. For the simulation of photon propagation through the WLS fibers we considered reflection, refraction, absorption, Rayleigh scattering, scintillation and Cerenkov emission as the relevant optical processes. A visualization of our set up in Geant4 is shown in Fig. 3.

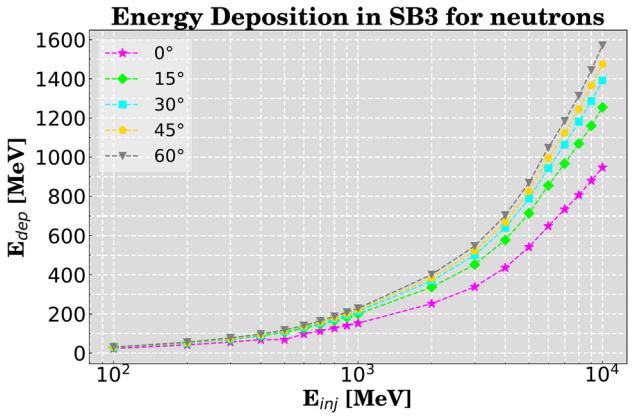

Fig. 4 E_{dep} of neutrons in the SB3 of the SciCRT, upon injection on the top of the SB1, with injection energies ranging from E_{inj} = 10^2 MeV to E_{inj} = 10^4 MeV and injection zenith angles θ = 0°, 15°, 30°, 45° and 60°

4 Simulation results

In order to characterize the detection response of the SciCRT active components we simulated the injection of 10^5 particles on top of the SB1 that propagated downward through the scintillation bars, interacting with the SciCRT active components (Fig. 3). Our results are the average detection efficiency of the SB3 and ML and the average energy deposition therein. For each particle species we used the injection zenith angles θ = 0°, 15°, 30°, 45° and 60° with injection energies ranging from E_{inj} = 10^2 MeV to E_{inj} = 10^4 MeV. In this way, our simulation covers the energies at which the secondary CR produced by LEGCR might arrive at the SN-CRO; also, the energy range below some GeV is of interest to study n_s.

4.1 Energy deposition

Our simulation results are shown in Figs. 4, 5, 6 and 7, corresponding to the average E_{dep} of neutrons, γ-rays, protons and electrons in the SB3 for injection zenith angles θ = 0°, 15°, 30°, 45° and 60° and injection energies ranging from E_{inj} = 10^2 MeV to E_{inj} = 10^4 MeV. Likewise, Fig. 8 shows the average E_{dep} of muons in the four ML with injection energies ranging from E_{inj} = 3×10^2 MeV to E_{inj} = 10^4 MeV.

Each point in Figs. 4, 5, 6, 7 and 8 represent the energy that a particle must have at the top of the SciCRT in order to deposit a specific amount of energy in the corresponding active components; for example, when neutrons impinge with θ = 0° on the top of the SciCRT with E_{inj} = 500 MeV, they deposit about 100 MeV in the SB3 (Fig. 4). The same reasoning follows for the E_{dep} in Figs. 5, 6, 7 and 8. An angular dependence is evident in all cases and is due to the longer paths that particles travel inside the SciCRT as θ increases. Such path lengthening results in an increased interaction rate and, consequently, a higher E_{dep}.

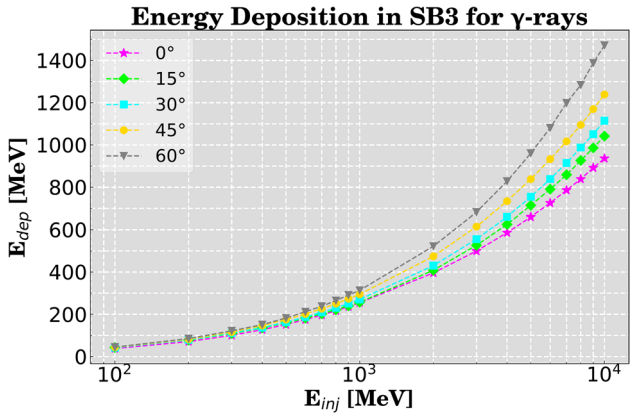

Fig. 5 E_{dep} of γ-rays in the SB3 of the SciCRT, upon injection on the top of the SB1, with injection energies ranging from $E_{inj} = 10^2$ MeV to $E_{inj} = 10^4$ MeV and injection zenith angles $\theta = 0°$, 15°, 30°, 45° and 60°

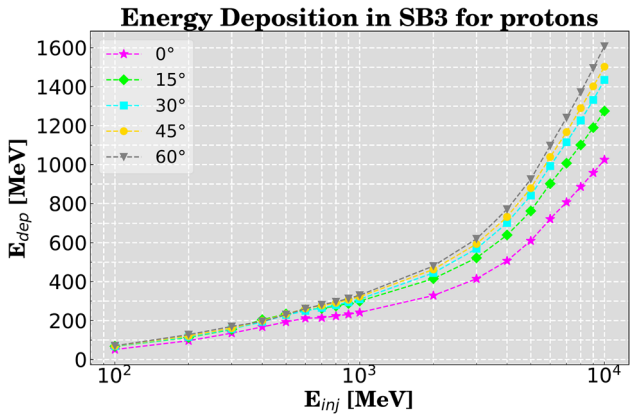

Fig. 6 E_{dep} of protons in the SB3 of the SciCRT, upon injection on the top of the SB1, with injection energies ranging from $E_{inj} = 10^2$ MeV to $E_{inj} = 10^4$ MeV and injection zenith angles $\theta = 0°$, 15°, 30°, 45° and 60°

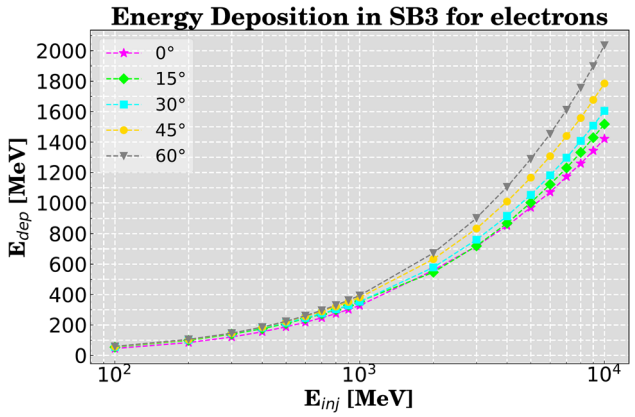

Fig. 7 E_{dep} of electrons in the SB3 of the SciCRT, upon injection on the top of the SB1, with injection energies ranging from $E_{inj} = 10^2$ MeV to $E_{inj} = 10^4$ MeV and injection zenith angles $\theta = 0°$, 15°, 30°, 45° and 60°

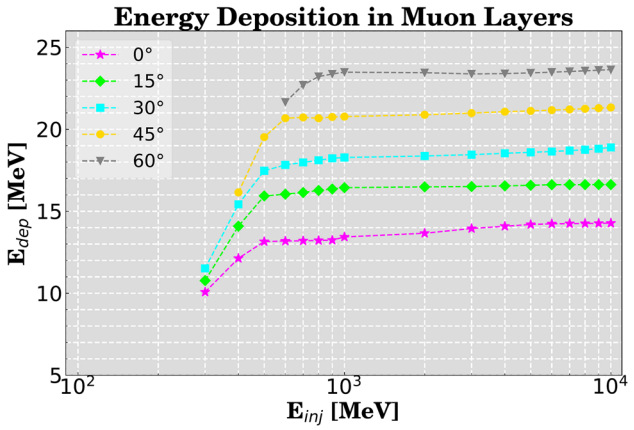

Fig. 8 E_{dep} of muons hitting the four ML of the SciCRT with injection energies ranging from $E_{inj} = 10^2$ MeV to $E_{inj} = 10^4$ MeV and injection zenith angles $\theta = 0°$, 15°, 30°, 45° and 60°. The plot starts at $E_{inj} = 300$ MeV according to the results obtained with Eq. 2

Superblock 3. Our simulation results suggest that a threshold for maximum E_{dep} for each particle and θ may be approximated for the SB3 based on the behavior of the curves in Figs. 4, 5, 6 and 7. As an example, in order to discern the detection of neutrons and γ-rays, it can be noted that, on average, neutrons impinging with $E_{inj} \sim 600$ MeV will have an $E_{dep} < 150$ MeV, whereas γ-rays with the same features will have $E_{dep} \geq 150$ MeV. Hence, a particle entering the top of the SciCRT that deposits $E_{dep} < 150$ MeV in the SB3 might be considered as a neutron with $E_{inj} \sim 600$ MeV and an analysis of its track should be applied for its identification. In such case, a neutron is expected to leave a hadronic track inside the SciCRT; on the other hand, a γ-ray would generate an electromagnetic track [11]. Thus, our results may be utilized as a complementary tool to study the particles detected by the SciCRT.

A similar simulation was developed for the SNT-SN in order to study the particle emission associated with an X17 solar flare; along with the analysis of the SNT-SN data, these results allowed to reconstruct the energy spectrum of primary particles over the Earth's atmosphere, [9,24]. In the case of n_s, this deconvolution provides unaltered information about the source in the solar atmosphere and thus allows to infer the energies at which charged particles were accelerated during a flare, [3].

Muon layers. Figure 8 shows the E_{dep} of muons in the ML. Unlike the particles injected in the SB3, muons have an E_{dep} that is nearly constant after a given E_{inj} value according to the injection angle θ. Such behavior is reached at $E_{dep} \sim$ 13 MeV, $\sim$ 16 MeV, $\sim$ 18 MeV, $\sim$ 21 MeV and $\sim$ 23 MeV for $\theta = 0°$, 15°, 30°, 45° and 60°, respectively. Taking into account the chemical composition of the plastic scintillator, muons have an ionization energy loss of about 1.8 MeV g^{-1} cm^2 in the ML when considered as Minimum Ionizing Par-

ticles (MIP), [28]; it must be pointed out that ionization is the dominant energy loss process for muons in the energy range used in our simulation (E < 100 GeV), [33]. Thus, in order to pass through the upper and lower ML vertically, muons need at least E_{inj} ~320 MeV at the top of the μ_A layer. However, for $\theta \neq 0°$ the net distance travelled inside the SciCRT is higher; therefore, the minimum energy (E_{min}) that muons require to reach the lower ML and leave signal increases and can be approximated according to:

$$E_{min} = \rho \times MIP \times \frac{h_{SciCRT}}{cos(\theta)}. \quad (2)$$

Equation 2 is essentially the Bethe-Bloch formula [28] and the SciCRT height is h_{SciCRT} = 166.4 cm, ρ = 1.08 g cm^{-3} is the plastic scintillator density, $MIP \sim 1.8$ MeV g^{-1} cm^2 [28], and θ is the zenith injection angle on the top of the μ_A layer. The corresponding E_{min} for θ = 15°, 30°, 45° and 60° are ~ 323 MeV, ~ 335 MeV, ~ 457 MeV and ~ 647 MeV, respectively. Above those energies, muons are able to traverse the whole SciCRT and the E_{dep} is almost constant for increasing E_{inj} as observed in Fig. 8. On the other hand, $E_{inj} \lesssim E_{min}$ would correspond to muons depositing energy only in the upper ML; however, these would not fulfill the four-fold trigger condition and would not be registered by the SciCRT. Therefore, according to the E_{min} calculations performed with Eq. 2, the curves in Fig. 8 start at E_{inj} = 3×10^2 MeV.

4.2 Detection efficiency

We simulated the WLS fibers and MAPMT's for the bars of the SB3 and ML taking into account the optical properties mentioned in Sect. 2; in this manner, we calculated the average detection efficiency ($\epsilon(E_{inj}, \theta)$) of the ML and of the SB3 as the ratio between the number of particles injected on top of SB1, with injection zenith angles θ = 0°, 15°, 30°, 45° and 60°, and the number of particles recorded in the MAPMT. The particles that we injected for the SB3 are neutrons, γ-rays, protons and electrons, in the energy range from E_{dep} = 10^2 MeV to E_{dep} = 10^4 MeV. Similarly, for the ML we injected muons with energies ranging from E_{dep} = 3×10^2 MeV to E_{dep} = 10^4 MeV. The results are normalized to 1 and are presented in Figs. 9, 10, 11, 12 and 13.

Superblock 3. Figures 9, 10, 11 and 12 show the angular variation of the $\epsilon(E_{inj}, \theta)$ since there is a curve for each θ that follows a dependence with the E_{inj}. Although such $\epsilon(E_{inj}, \theta)$ is similar for all cases, particle identification issues regarding contamination signals may be solved with the analysis of tracks inside the SciCRT. The curves for θ = 45° and 60° in Figs. 10 and 12 suggest that the γ-rays and electrons detected by the SB3 of the SciCRT arrive most likely from slanted trajectories. Considering the detection principle of the SciCRT, the enhancement in the $\epsilon(E_{inj}, \theta)$ for θ = 60° is explained by

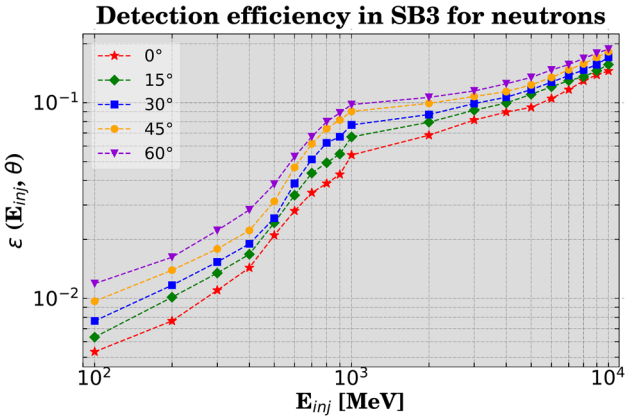

Fig. 9 Detection efficiency of the SB3 for neutrons, upon injection on the top of the SB1, with injection energies ranging from E_{inj} = 10^2 MeV to E_{inj} = 10^4 MeV and injection zenith angles θ = 0°, 15°, 30°, 45° and 60°

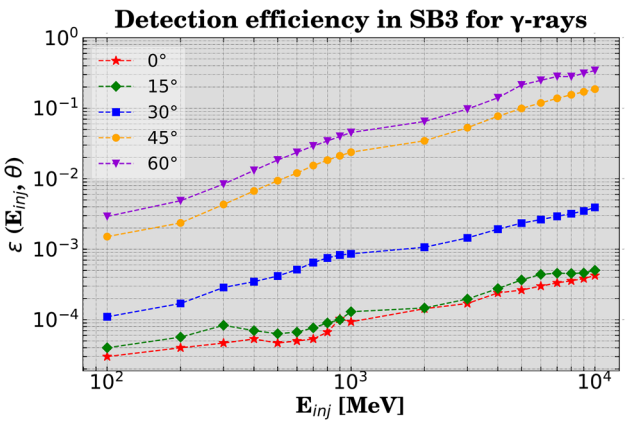

Fig. 10 Detection efficiency of the SB3 for γ-rays, upon injection on the top of the SB1, with injection energies ranging from E_{inj} = 10^2 MeV to E_{inj} = 10^4 MeV and injection zenith angles θ = 0°, 15°, 30°, 45° and 60°

the electron E_{dep} since it is higher than for the other particles in such cases (Fig. 7). Our results are in agreement with the simulation performed by [23] and show the explicit angular dependence of the $\epsilon(E_{inj}, \theta)$.

Muon layers. In order for the ML to detect a muon, a signal has to be received in at least one of the MAPMT of the μ_A, μ_B, μ_A' and μ_B' plates. We required such four-fold coincidence condition in our simulation; in this manner, Fig. 13 shows the total $\epsilon(E_{inj}, \theta)$ of the four ML. A preliminary version of this plot was developed in [34]; nevertheless, in this work we increased the muon energy range and the updated results align properly with the preliminary version for the interval between E_{inj} = 10^2 MeV and E_{inj} = 10^3 MeV.

As θ increases, muons traverse the SciCRT following a longer path from the μ_A and μ_B plates to the μ_A' and μ_B' plates. These longer paths increase the interaction rate; whereby the scintillation emission also increases, leading to

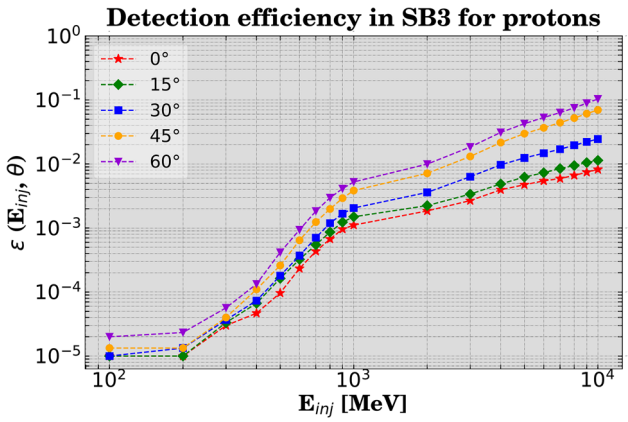

Fig. 11 Detection efficiency of the SB3 for protons, upon injection on the top of the SB1, with injection energies ranging from $E_{inj} = 10^2$ MeV to $E_{inj} = 10^4$ MeV and injection zenith angles $\theta = 0°$, 15°, 30°, 45° and 60°

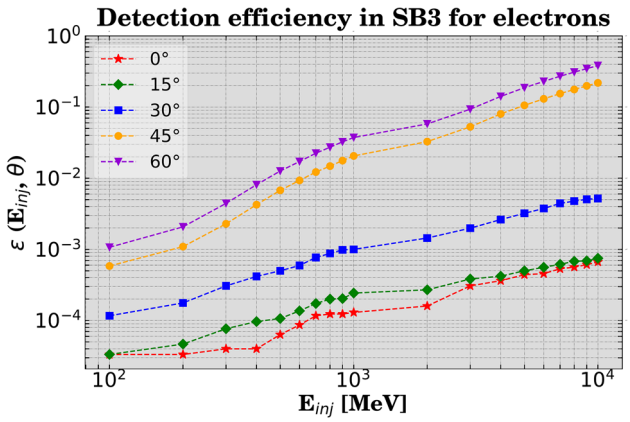

Fig. 12 Detection efficiency of the SB3 for electrons, upon injection on the top of the SB1, with injection energies ranging from $E_{inj} = 10^2$ MeV to $E_{inj} = 10^4$ MeV and injection zenith angles $\theta = 0°$, 15°, 30°, 45° and 60°

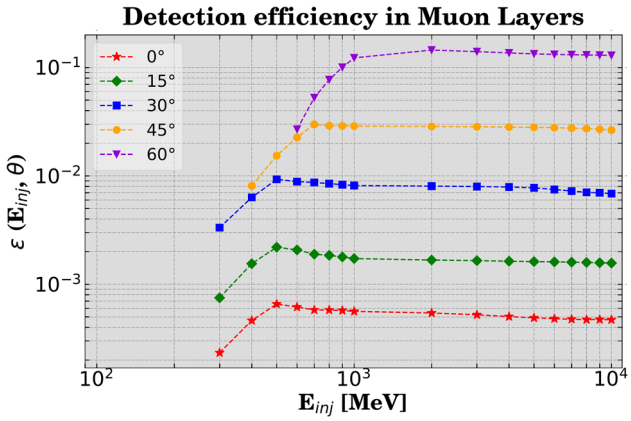

Fig. 13 Detection efficiency of the ML for muons with injection energies ranging from $E_{inj} = 300$ MeV to $E_{inj} = 10^4$ MeV and injection zenith angles $\theta = 0°$, 15°, 30°, 45° and 60°. The plot starts at $E_{inj} = 300$ MeV according to the calculations carried out with Eq. 2. Updated from [34]

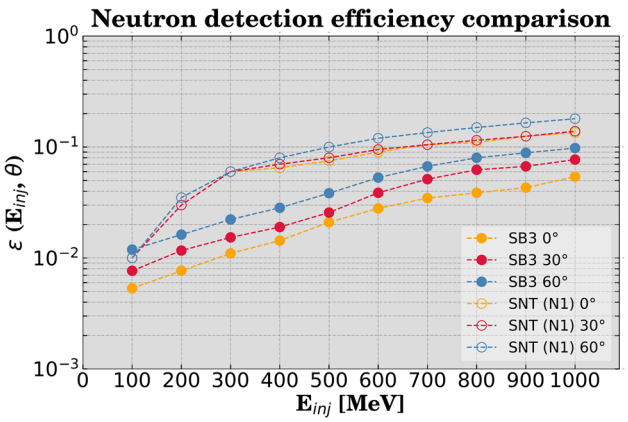

Fig. 14 Comparison of neutron detection efficiency between the SciCRT and the SNT-SN. Hollow marks indicate the detection efficiency of the N1 channel of the SNT-SN (neutral particles with $E_{dep} > 30$ MeV, [9]) and the full marks represent the detection efficiency of the SB3 of the SciCRT

a higher detection probability. As a result, Fig. 13 implies that detection of muons impinging the top of the SciCRT with $\theta = 45°$ and 60° is significantly more efficient than for lower injection zenith angles $\theta = 0°$, 15° and 30°; therefore, it is highly probable that the muons detected by the SciCRT are mostly coming from slanted trajectories. In corcondance with Fig. 8 and the calculations performed with Eq. 2, the penetration power of muons is also observed in Fig. 13 as the increase observed between $E_{inj} = 300$ MeV and $E_{inj} = 600$ MeV for all θ correspond to muons with $E_{dep} \gtrsim E_{min}$. For increasing E_{inj}, muons are able to cross the whole SciCRT without further E_{dep}; thus, the $\epsilon(E_{inj}, \theta)$ decreases until reaching a nearly constant value and this is observed for all θ.

4.3 SciCRT and SNT-SN comparison

Given that the main goal of both the SciCRT and the SNT-SN is neutron detection, Fig. 14 compares their neutron $\epsilon(E_{inj}, \theta)$ for the angles and energies simulated for the SNT-SN in [9]. The curves for the SNT-SN (hollow marks) represent the $\epsilon(E_{inj}, \theta)$ of the neutral channel N1, which detects neutral particles with the widest E_{dep} resolution ($E_{dep} > 30$ MeV). Similarly, the curves for the SciCRT (full marks) depict the $\epsilon(E_{inj}, \theta)$ of the SB3. It can be observed that the N1 channel of the SNT-SN outperforms the neutron detection of the SB3 of the SciCRT; however, it must be noted that the SB3 represents just 1/8 of the SciCRT counting rates.

Figures 15, 16 and 17 compare the SB3 detection efficiency for γ-rays, protons and electrons, respectively, with the SNT-SN detection efficiency obtained in [9]. The hollow marks in Figs. 16 and 17 represent the efficiency of the C1 channel of the SNT-SN. Such channel detects charged particles with the widest E_{dep} resolution ($E_{dep} > 30$ MeV).

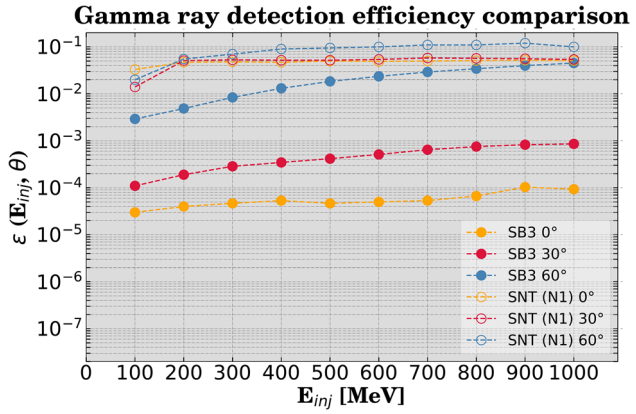

Fig. 15 Comparison of γ-rays detection efficiency between the SciCRT and the SNT-SN. Hollow marks indicate the detection efficiency of the N1 channel of the SNT-SN (neutral particles with $E_{dep} > 30$ MeV, [9]) and the full marks represent the detection efficiency of the SB3 of the SciCRT

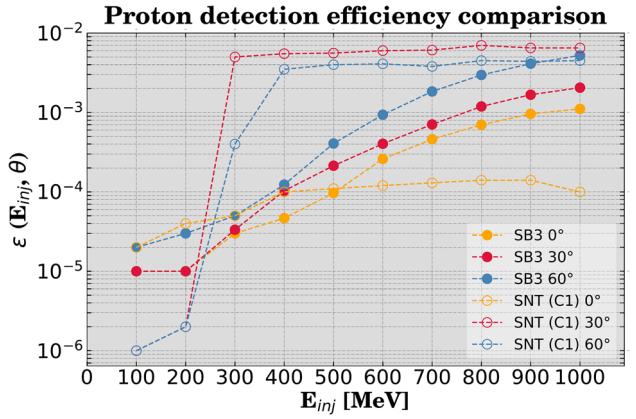

Fig. 16 Comparison of proton detection efficiency between the SciCRT and the SNT-SN. Hollow marks indicate the detection efficiency of the C1 channel of the SNT-SN (charged particles with $E_{dep} > 30$ MeV, [9]) and the full marks represent the detection efficiency of the SB3 of the SciCRT

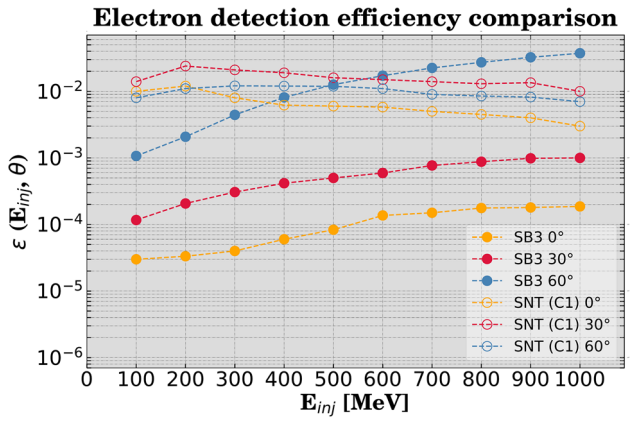

Fig. 17 Comparison of electron detection efficiency between the SciCRT and the SNT-SN. Hollow marks indicate the detection efficiency of the C1 channel of the SNT-SN (charged particles with $E_{dep} > 30$ MeV, [9]) and the full marks represent the detection efficiency of the SB3 of the SciCRT

According to Fig. 16, the $\epsilon(E_{inj}, \theta)$ for protons of the SB3 and the C1 channel are in similar orders of magnitude; however, the SB3 detects protons more efficiently than the C1 channel only for and $E_{inj} \geq 600$ MeV and $\theta = 0°$

Excluding the cases for $\theta = 0°$ and 30°, it can be observed that the SB3 and the N1 channel have similar $\epsilon(E_{inj}, \theta)$ for γ-rays (Fig. 15). Likewise, the $\epsilon(E_{inj}, \theta)$ of the SB3 and the C1 channel for electrons is in similar orders of magnitude; in addition, the $\epsilon(E_{inj}, \theta)$ of the SB3 for electrons impinging with $\theta = 60°$ is higher than the C1 channel of the SNT-SN for $E_{inj} \geq 600$ MeV (Fig. 17). Such enhancement in the $\epsilon(E_{inj}, \theta)$ for $\theta = 60°$ in both cases is attributed to the E_{dep} of electrons, which is the highest in the SB3 according to Fig. 7, since a higher E_{dep} implies a higher scintillation emission and also a higher detection probability.

For the majority of E_{inj} and θ used in the simulation, the N1 channel and the C1 channel of the SNT-SN have a higher $\epsilon(E_{inj}, \theta)$ than the SB3 of the SciCRT. Such differences are attributed to the different set ups of the SN-SNT and the SciCRT. The plastic scintillator of the SN-SNT is 30 cm thick, which accounts for its particle detection efficiency. In the case of the SciCRT, each SB is 21 cm thick and the particles reaching the SB3 must traverse the 42 cm thick corresponding to the SB1 and SB2. Compared to the SNT-SN, this longer path implies a greater attenuation and energy loss; therefore, the detection probability of the SB3 decreases significantly. Thus, the SB3 alone does not surpass the detection capability of the C1 channel and N1 channel of the SNT-SN; nevertheless, our simulation results show that the SB3 performs properly in the detection of secondary CR and might be used to optimize the results of ongoing research such as the work presented in [35].

5 Concluding remarks

We have calculated the E_{dep} of neutrons, γ-rays, protons, electrons and muons in the active components of the SciCRT, for energies ranging from $E_{inj} = 10^2$ MeV to $E_{inj} = 10^4$ MeV and injection zenith angles $\theta = 0°$, 15°, 30°, 45° and 60°. Since it is possible to deconvolute the energy of a primary particle, over the Earth's atmosphere, from a detector counting rate [36] our results may be used as a basis for the energy estimation of particles accelerated in the solar atmosphere during a solar flare using the SciCRT detection response.

We also calculated the detection efficiency $\epsilon(E_{inj}, \theta)$ of the SciCRT active components. The calculation for the ML carried out in [34] was improved, yielding satisfactory results.

In this manner, we have characterized the detection response of the active components of the SciCRT and our results show that, at its current state, it performs properly in the detection of particles with energies ranging from $E_{inj} =$

10^2 MeV to $E_{inj} = 10^4$ MeV. While the SNT-SN detection capacity remains superior, it is crucial to note that the SciCRT performance is still under constant improvements; therefore, based on our simulaton results, we expect that the whole array of SB's will surpass the detection capabilities of the SNT-SN. As the SciCRT electronics conclude its optimizations, we will evaluate and extend the simulations presented in this work; which, combined with SciCRT's capability to record particle tracks, will enable us to study the arrival of secondary cosmic rays associated with the solar flares expected for the forthcoming maximum of solar cycle 25.

Acknowledgements This work was partially supported by AEM-2018-01-A3-S-63804, Fondo Sectorial CONAHCyT-AEM, CONAHCyT-LN293598. This work was also partially supported by Programa Espacial Universitario (PEU), Universidad Nacional Autónoma de México (UNAM). F. Monterde-Andrade is a PhD student from Programa de Doctorado en Ciencias de la Tierra, UNAM and wish to thank CONAHCyT for granting a fellowship to perform this research. Morales-Olivares O. G. thanks to CONAHCyT for granting a postdoctoral fellowship to perform this research.

Data Availability Statement This manuscript has no associated data. [Author's' comment: The code/software generated during and/or analysed during the current study is available from the corresponding author on reasonable request].

Code Availability Statement Code/software will be made available on reasonable request. [Author's comment: Data sharing not applicable to this article as no datasets were generated or analysed during the current study].

Open Access This article is licensed under a Creative Commons Attribution 4.0 International License, which permits use, sharing, adaptation, distribution and reproduction in any medium or format, as long as you give appropriate credit to the original author(s) and the source, provide a link to the Creative Commons licence, and indicate if changes were made. The images or other third party material in this article are included in the article's Creative Commons licence, unless indicated otherwise in a credit line to the material. If material is not included in the article's Creative Commons licence and your intended use is not permitted by statutory regulation or exceeds the permitted use, you will need to obtain permission directly from the copyright holder. To view a copy of this licence, visit http://creativecommons.org/licenses/by/4.0/.
Funded by SCOAP[3].

References

1. L. Dorman, *Solar Neutrons and Related Phenomena*, vol. 365 (Springer Science & Business Media, Berlin, 2010)
2. F.M. Gonzalez, E. Fries, C. Cude-Woods, T. Bailey, M. Blatnik, L. Broussard, N. Callahan, J. Choi, S. Clayton, S. Currie et al., Improved neutron lifetime measurement with ucn τ. Phys. Rev. Lett. **127**(16), 162501 (2021)
3. J.F. Valdés-Galicia, Y. Muraki, K. Watanabe, Y. Matsubara, T. Sako, L.X. González, O. Musalem, A. Hurtado, Solar neutron events as a tool to study particle acceleration at the Sun. Adv. Space Res. **43**(4), 565–572 (2009)
4. E. Ortiz, R. García, M. Anzorena, J. Valdés-Galicia, L. González, A. Hurtado, O. Musalem, R. Taylor, O. Morales-Olivares, T. Quintanar, Solar neutron event recorded by a muon telescope in Mexico City on November 4, 2003. Adv. Space Res. **73**(9), 4853–4858 (2024). (**online**)
5. K. Watanabe, Solar neutron events associated with large solar flares in solar cycle 23, Ph.D. thesis, University of Nagoya, Nagoya (2005)
6. T. Sako, K. Watanabe, Y. Muraki, Y. Matsubara, H. Tsujihara, M. Yamashita, T. Sakai, S. Shibata, J.F. Valdés-Galicia, L.X. González et al., Long-lived solar neutron emission in comparison with electron-produced radiation in the 2005 September 7 solar flare. Astrophys. J. Lett. **651**(1), L69 (2006)
7. Y. Muraki, D. Lopez, K. Koga, F. Kakimoto, T. Goka, L. González, S. Masuda, Y. Matsubara, H. Matsumoto, P. Miranda et al., Simultaneous observation of solar neutrons from the International Space Station and high mountain observatories in association with a flare on July 8, 2014. Sol. Phys. **291**, 1241–1265 (2016)
8. J.F. Valdés-Galicia, Y. Muraki, H. Tsujihara, T. Sako, O. Musalem, A. Hurtado, L.X. González, Y. Matsubara, K. Watanabe, N. Hirano et al., An improved Solar Neutron Telescope installed at a very high altitude in Mexico. Nucl. Instrum. Methods Phys. Res. Sect. A **535**(3), 656–664 (2004)
9. L.X. González, F. Sánchez, J.F. Valdés-Galicia, Geant4 simulation of the Solar Neutron Telescope at Sierra Negra, Mexico. Nucl. Instrum. Methods Phys. Res. Sect. A **613**(2), 263–271 (2010)
10. J. Newton-Bosch, L.X. González, J.F. Valdés-Galicia, O.G. Morales-Olivares, Y. Muraki, S. Shibata, Y. Matsubara, T. Sako, K. Watanabe, M. Sergeeva, F. Monterde-Andrade, S. Perea-Contreras, E. Ortiz, O. Musalem, A. Hurtado, R. Taylor, Atmospheric electric field effects on cosmic rays detected by the Solar Neutron Telescope at Sierra Negra. J. Atmos. Sol. Terr. Phys. 106156 (2023). [Online]
11. Y. Nagai, Y. Matsubara, Y. Itow, T. Sako, D. Lopez, Y. Sasai, T. Itow, K. Munakata, C. Kato, M. Kozai et al., First cosmic-ray measurements by the SciCRT solar neutron experiment in Mexico. Astropart. Phys. **59**, 39–46 (2014)
12. T. Sako, Y. Muraki, N. Hirano, H. Tsuchiya, Super Solar Neutron Telescope for the next solar maximum, in *Proceedings of the 28th International Cosmic Ray Conference. July 31–August 7, 2003. Tsukuba, Japan. Under the auspices of the International Union of Pure and Applied Physics (IUPAP)*, vol. 6, ed. by T. Kajita, Y. Asaoka, A. Kawachi, Y. Matsubara, M. Sasaki (2003), p. 3437
13. K. Nitta, E. Aliu, S. Andringa, S. Aoki, S. Choi, U. Dore, X. Espinal, J. Gomez-Cadenas, R. Gran, M. Hasegawa et al., The K2K Scibar detector. Nucl. Instrum. Methods Phys. Res. Sect. A **535**(1–2), 147–151 (2004)
14. K. Hiraide, The Scibar detector at FNAL booster neutrino experiment. Nucl. Phys. B (Proc. Suppl.) **159**, 85–90 (2006)
15. Y. Sasai, Y. Nagai, Y. Itow, Y. Matsubara, T. Sako, D. Lopez, T. Itow, K. Munakata, C. Kato, M. Kozai et al., Performance of the Scibar Cosmic Ray Telescope (SciCRT) toward the detection of high-energy solar neutrons in solar cycle 24. Earth Planets Space **66**(1), 1–8 (2014)
16. Y. Sasai, *Sensitivity studies on the Scibar Cosmic Ray Telescope (SciCRT) at Full Performance for Ground-based Observations of Solar Neutrons* (Nagoya University, Nagoya, 2017)
17. E. Ortiz, J.F. Valdés-Galicia, Y. Matsubara, Y. Nagai, A. Hurtado, O. Musalem, R. García, M. Anzorena, L.X. González, Y. Itow et al., Observation of cosmic ray hadrons at the top of the Sierra Negra volcano in Mexico with the SciCRT prototype. Adv. Space Res. **58**(10), 2018–2025 (2016)
18. M.S. Longair, *High Energy Astrophysics* (Cambridge University Press, Cambridge, 2011)
19. J.B. Birks, *The Theory and Practice of Scintillation Counting: International Series of Monographs in Electronics and Instrumentation*, vol. 27 (Elsevier, Amsterdam, 2013)

20. E. Ortiz, J. Valdés-Galicia, A. Hurtado, R. García, M. Anzorena, O. Musalem, L. González, Y. Matsubara, Y. Muraki, Y. Itow et al., Neutron and gamma-ray fluxes measured by SciCRT prototype at the top of Sierra Negra Volcano, Mexico. Revista mexicana de física **65**(5), 545–553 (2019)
21. K. Koga, Y. Muraki, S. Masuda, S. Shibata, H. Matsumoto, H. Kawano, Measurement of solar neutrons on 05 March 2012, using a fiber-type neutron monitor onboard the attached payload to the iss. Sol. Phys. **292**, 1–16 (2017)
22. G. Ros, G. Sáez-Cano, G. Medina-Tanco, A.D. Supanitsky, On the design of experiments based on plastic scintillators using geant4 simulations. Radiat. Phys. Chem. **153**, 140–151 (2018)
23. M. Anzorena, R. Garcia, J.F. Valdés-Galicia, Y. Matsubara, Y. Itow, T. Sako, T. Kawabata, E. Ortiz, R. Taylor, A. Hurtado et al., Simulation and experimental validation of optimum read-out electronics design for Scintillator bar Cosmic Ray Telescope. Nucl. Instrum. Methods Phys. Res. Sect. A **991**, 165019 (2021)
24. L.X. González, J.F. Valdés-Galicia, F. Sánchez, Y. Muraki, T. Sako, K. Watanabe, Y. Matsubara, Y. Nagai, S. Shibata, T. Sakai et al., Re-evaluation of the neutron emission from the solar flare of 2005 September 7, detected by the Solar Neutron Telescope at Sierra Negra. Astrophys. J. **814**(2), 136 (2015)
25. F. Monterde-Andrade, L.X. González, J.F. Valdés-Galicia, O.G. Morales-Olivares, Y. Muraki, Y. Matsubara, T. Sako, K. Watanabe, S. Shibata, M.A. Sergeeva, A. Hurtado, O. Musalem, R. Taylor, J. Newton-Bosch, S. Perea-Contreras, E. Ortiz, Simulation of solar neutron flux in the earth's atmosphere for three selected flares. Astropart. Phys. **145**, 102780 (2023). (**online**)
26. D. Heck, J. Knapp, J.N. Capdevielle, G. Schatz, T. Thouw, CORSIKA: a Monte Carlo code to simulate extensive air showers (1998)
27. F. Monterde-Andrade, L.X. González, J.F. Valdés-Galicia, J. Newton-Bosch, S. Perea-Contreras, Y. Muraki, Y. Matsubara, T. Sako, K. Watanabe, S. Shibata et al., Influx of particles in the atmosphere after an intense solar flare: a simulation for hadron propagation, in *Atmosphere, Ionosphere, Safety* (2023), pp. 99–101
28. R.L. Workman et al., Review of particle physics. PTEP **2022**, 083C01 (2022)
29. S. Agostinelli, J. Allison, K.A. Amako, J. Apostolakis, H. Araujo, P. Arce, M. Asai, D. Axen, S. Banerjee, G. Barrand et al., Geant4—a simulation toolkit. Nucl. Instrum. Methods Phys. Res. Sect. A Accelerators Spectrom. Detect. Assoc. Equip. **506**(3), 250–303 (2003)
30. R. Garcia, M. Anzorena, J.F. Valdés-Galicia, Y. Matsubara, T. Sako, E. Ortiz, A. Hurtado, R. Taylor, O. Musalem, L.X. González et al., Particle identification and analysis in the SciCRT using machine learning tools. Nucl. Instrum. Methods Phys. Res. Sect. A **1003**, 165326 (2021)
31. A.V. Ivantchenko, V.N. Ivanchenko, J.-M.Q. Molina, S.L. Incerti, Geant4 hadronic physics for space radiation environment. Int. J. Radiat. Biol. **88**(1–2), 171–175 (2012). https://doi.org/10.3109/09553002.2011.610865. (**online**)
32. J. Allison, K. Amako, J. Apostolakis, P. Arce, M. Asai, T. Aso, E. Bagli, A. Bagulya, S. Banerjee, G. Barrand, B. Beck, A. Bogdanov, D. Brandt, J. Brown, H. Burkhardt, P. Canal, D. Cano-Ott, S. Chauvie, K. Cho, G. Cirrone, G. Cooperman, M. Cortés-Giraldo, G. Cosmo, G. Cuttone, G. Depaola, L. Desorgher, X. Dong, A. Dotti, V. Elvira, G. Folger, Z. Francis, A. Galoyan, L. Garnier, M. Gayer, K. Genser, V. Grichine, S. Guatelli, P. Guèye, P. Gumplinger, A. Howard, I. Hřivnáčová, S. Hwang, S. Incerti, A. Ivanchenko, V. Ivanchenko, F. Jones, S. Jun, P. Kaitaniemi, N. Karakatsanis, M. Karamitros, M. Kelsey, A. Kimura, T. Koi, H. Kurashige, A. Lechner, S. Lee, F. Longo, M. Maire, D. Mancusi, A. Mantero, E. Mendoza, B. Morgan, K. Murakami, T. Nikitina, L. Pandola, P. Paprocki, J. Perl, I. Petrović, M. Pia, W. Pokorski, J. Quesada, M. Raine, M. Reis, A. Ribon, A. Ristić Fira, F. Romano, G. Russo, G. Santin, T. Sasaki, D. Sawkey, J. Shin, I. Strakovsky, A. Taborda, S. Tanaka, B. Tomé, T. Toshito, H. Tran, P. Truscott, L. Urban, V. Uzhinsky, J. Verbeke, M. Verderi, B. Wendt, H. Wenzel, D. Wright, D. Wright, T. Yamashita, J. Yarba, H. Yoshida, Recent developments in geant4. Nucl. Instrum. Methods Phys. Res. Sect. A Accelerators Spectrom. Detectors Assoc. Equip. **835**, 186–225 (2016) **(online)**
33. P.K. Grieder, *Cosmic Rays at Earth* (Elsevier, Amsterdam, 2001)
34. F. Monterde Andrade, L.X. González, J.F. Valdés Galicia, J. Newton-Bosch, O.G. Morales Olivares, Y. Matsubara, Y. Itow, T. Sako, T. Kawabata, E. Ortiz, A. Hurtado, O. Musalem, R. Taylor, K. Munakata, C. Kato, W. Kihara, Y. Ko, S. Shibata, H. Takamaru, A. Oshima, T. Koi, H. Kojima, H. Tsuchiya, K. Watanabe, M. Kozai, Y. Nakamura, Preliminary Simulation of the Scibar Cosmic Ray Telescope (SciCRT) at Sierra Negra, in *Proceedings of 38th International Cosmic Ray Conference—PoS(ICRC2023)*, vol. 444 (2023), p. 1273
35. J. Newton-Bosch, L.X. González, J.F. Valdés-Galicia, O.G. Morales-Olivares, Y. Muraki, S. Shibata, Y. Matsubara, T. Sako, K. Watanabe, F. Monterde Andrade, S. Perea-Contreras, E. Ortiz, O. Musalem, A. Hurtado, R. Taylor, Geomagnetic Storm Effects on the Solar Neutron Telescope at Sierra Negra, Mexico, in *Proceedings of 38th International Cosmic Ray Conference—PoS(ICRC2023)*, vol. 444 (2023), p. 1272
36. Y. Muraki, K. Murakami, M. Miyazaki, K. Mitsui, S. Shibata, S. Sakakibara, T. Sakai, T. Takahashi, T. Yamada, K. Yamaguchi, Observation of solar neutrons associated with the large flare on 1991 June 4. Astrophys. J. **400**, L75–L78 (1992)